Investigating beach erosion related with tsunami sediment transport at Phra Thong Island, Thailand caused by the 2004 Indian Ocean tsunami

Ryota Masaya [1], Anawat Suppasri [2], Kei Yamashita [2], Fumihiko Imamura [2], Chris Gouramanis [3] and Natt Leelawat [4, 5]

[1]Graduate School of Engineering, Tohoku University, Aoba 6-6-06, Aoba, Sendai 980-0845, Japan
[2]International Research Institute of Disaster Science, Tohoku University, 468-1 Aoba, Aramaki-Aza, Aoba, Sendai 980-0845, Japan
[3]Department of Geography, National University of Singapore, 1 Arts Link, Singapore 117570, Singapore
[4]Department of Industrial Engineering, Faculty of Engineering, Chulalongkorn University, Phayathai Road, Pathumwan, Bangkok 10330, Thailand
[5]Disaster and Risk Management Information Systems Research Group, Chulalongkorn University, Phayathai Road, Pathumwan, Bangkok 10330, Thailand
*Corresponding author.
E-mail address: ryota.masaya.r6@dc.tohoku.ac.jp (Ryota Masaya)

Abstract

The 2004 Indian Ocean Tsunami and the 2011 Great East Japan earthquake and tsunami caused large-scale topographic changes in coastal areas. Whereas much research has focused on coastlines that have or had large human populations, little focus has been paid on coastlines that have little or no infrastructure. The importance of examining erosional and depositional mechanisms of tsunami events lies in the rapid reorganisation that coastlines must undertake immediately after an event. A thorough understanding of the pre-event conditions is paramount to understanding the natural reconstruction of the coastal environment. This study examines the location of sediment erosion and deposition during the 2004 Indian Ocean Tsunami event on the relatively pristine Phra Thong Island, Thailand. Coupled with satellite imagery, we use numerical simulations and sediment transportation models to determine the locations of significant erosion and the areas where much of that sediment was redeposited during the tsunami inundation and backwash processes. Our modelling approach suggests that beaches located in two regions on Phra Thong Island were significantly eroded by the 2004 tsunami, predominantly during the backwash phase of the first and largest wave to strike the island. Although 2004 tsunami deposits are found on the island, we demonstrate that most of the sediment was deposited in the shallow coastal area, facilitating quick recovery of the beach when normal coastal processes resumed.

1. Introduction

The 2004 Indian Ocean Tsunami and the 2011 Great East Japan earthquake and tsunami caused large-scale geomorphologic changes in coastal areas during the erosional phases of inflow and outflow (Pari

et al., 2008; Goto et al., 2011a; Tanaka et al., 2011; Haraguchi et al., 2012; Hirao et al., 2012; Udo et al., 2013; Imai et al., 2015). In each tsunami event, the erosional phases translocated sediments onshore and offshore, and primed the coastal zone for rapid (months to decades) recovery (Choowong et al., 2009; Ali and Narayama, 2015; Udo et al., 2016; Mieda et al., 2017; Koiwa et al., 2018). However, little information exists to identify real-time sediment dynamics during the erosional and depositional phases of tsunami events. In particular, erosive phases mobilize sediments into the onshore (e.g. Jankaew et al. 2008; Gouramanis et al. 2017) and offshore environments (e.g. Feldens et al 2009). Following the tsunami event, both offshore environment and coastal environments are primed for natural processes to resume and redistribute sediments onshore to restore the coastal environment to similar pre-tsunami configurations.

However, in many regions, such as the area affected by the 2011 tsunami, extensive engineering interventions (e.g. levee construction and land level raising) are affecting the natural recovery processes of the coastal zone. In Japan, many locations have not undergone or been allowed to recover naturally (Udo et al., 2016; Koiwa et al., 2018), as engineering interventions have taken precedence over natural recovery processes.

Along highly developed and populated coasts that have been affected by tsunami, e.g. Japan, plans for coastal reconstruction and defenses are typically formulated shortly after a tsunami, preventing natural recovery processes (Suppasri et al., 2016). These political and engineering interventions make it difficult to observe or predict the natural recovery processes of coastal areas.

Before an understanding of the recovery processes of a tsunami-affected coastal zone can be achieved, a thorough understanding of the sediment budget must be determined. The relocation of sediments during the main tsunami erosion and deposition phases establishes the pre-recovery or baseline conditions upon which natural processes can act to facilitate the recovery of the coastal zone. To determine the locations of sediment deposition during a tsunami event, the sediment transport dynamics during the tsunami must be defined.

Unfortunately, real-time data from observations has not been possible to establish quantitative estimates of sediment erosion and deposition during a tsunami event, though qualitative spatial patterns of sediment process (Udo et al., 2016; Yamashita et al., 2016) have been examined through analyze of video footage. Prior studies have mainly estimated sediment transport dynamics, such as erosion and sediment deposition through remote sensing (e.g. Fagherazzi and Du 2008, Choowong et al., 2009; Liew et al., 2010), and sedimentological and stratigraphic analysis (e.g. Paris et al. 2007; Hawkes et al. 2007; Switzer et al. 2012). However, the information obtained regarding the final results of the sediment transport process is limited. It is difficult to obtain information on where sediment has eroded and deposited (e.g. Pham et al., 2018), and whether topographic changes caused by the local sediment runoff or deposition are the results of action from inflow or backwash (e.g. Choowong et al., 2009; Paris et al 2007; Switzer et al. 2012). This information determines the sediment budget in the system before and after the tsunami and is therefore important for considering geomorphic recovery.

Numerical simulations using wave dynamics of an area can reproduce spatial-temporal variations of

77 the sediment mobility and deposition and can effectively model the sediment transport process using
78 the wave and sediment characteristics of the natural system. In recent years, the numerical modeling of
79 tsunami sediment transport has been developed (e.g. Takahashi et al., 2000), improved (e.g. Takahashi
80 et al., 2011; Apotsos et al., 2011a; Li et al., 2013; Morishita and Takahashi, 2014; Yamashita et al.,
81 2018) and applied in the field (e.g. Gelfenbaun et al., 2007; Takahashi et al., 2008; Apotsos et al., 2011b;
82 Apotsos et al., 2011c; Gusman et al., 2012; Li et al., 2014; Arimitsu et al., 2017; Yamashita et al., 2017),
83 and reproducibility has been confirmed by comparison between the calculated and measured values
84 (e.g. Li et al., 2012; Ranasinghe et al., 2013; Sugawara et al., 2014a; Yamashita et al., 2015; Yamashita
85 et al., 2016).
86 An important consideration in the sediment dynamics during catastrophic marine events (e.g. typhoon
87 and tsunami) is the degree of development and human modification of the coastal zone prior to the
88 event. Artificial structures, such as sea walls, roads and buildings interfere with washover processes,
89 and these areas are often targeted from reconstruction and rehabilitation through rapid engineering
90 reconstruction. Little is known about the recovery processes in sparsely developed and unpopulated
91 areas. As such, the largely, anthropogenically-undisturbed Phra Thong Island, western Thailand, is an
92 ideal location to model the sediment dynamics, coastal erosion and deposition following a major
93 tsunami event.
94 The main objective of this study is to investigate the short term conditions of sediment transport such
95 as erosional and depositional process and establishes the baseline sediment conditions that led to further
96 investigation of the long term recovery of the Phra Thong Island coastline after the 2004 IOT. We used
97 tsunami sediment transport calculations to spatio-temporally reproduce the sediment transport
98 processes occurring during the tsunami and identify zones of sediment deposition in the offshore and
99 onshore areas and validate these modelling results with published observational data of the 2004 IOT
100 deposits on the island. Due to the largely natural environment, Phra Thong Island is a rare case that is
101 useful for verifying tsunami sediment transport models where few artificial features can generate model
102 uncertainties.
103 Examining the sediment transport processes on Phra Thong Island is also expected to elucidate
104 phenomena, improve numerical calculation models for the future and is applicable to other areas.
105 Furthermore, at least three palaeotsunami deposits were identified in areas impacted by the 2004 IOT
106 on Phra Thong Island (Jankaew et al., 2008; Sawai et al., 2009; Fujino et al., 2009; Fujino et al., 2010;
107 Prendergast et al. 2012; Brill et al., 2012a, b; Gouramanis et al., 2017; Pham et al., 2018). Thus,
108 clarifying the sediment transport conditions of the 2004 tsunami will also be important for future
109 estimations of history, scope and cause of older tsunamis on Phra Thong Island and elsewhere in the
110 coastal areas of the Indian Ocean.
111
112

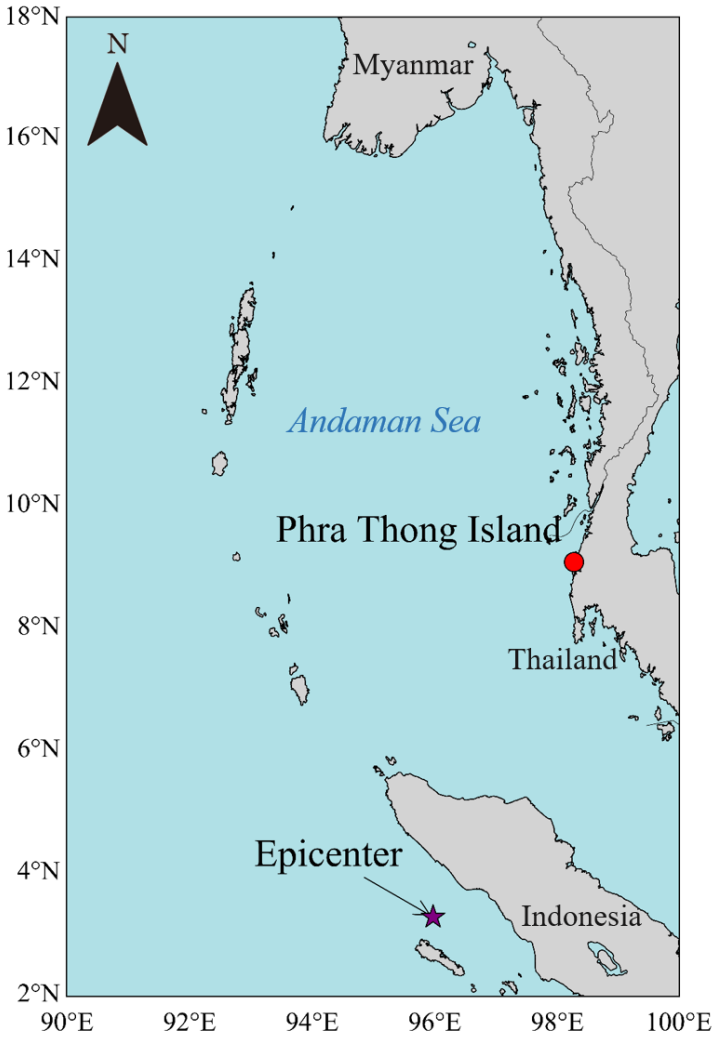

Figure 1 Location of Phra Thong Island

2. Setting and method

2.1. *Phra Thong Island, Thailand*

During the 2004 IOT, a wave of approximately 7 m inundated the northern portion of Phra Thong Island (Fig. 1) and measurements up to 20 m were recorded from the southernmost tip of the island (Jankaew et al. 2008). Over 70 people were lost and a village of 100 households disappeared. Geomorphologically, the western coast of the island has a beach ridge sequence trending parallel to the coast, which formed during the sea level regression following mid-Holocene sea level highstand at about 6,000 years ago (Brill et al. 2015). The eastern shore of the island is extensively covered by mangroves along the shores of tidal channels. The island has a tropical climate. Additionally, palaeotsunami deposits are preserved in swales in the beach ridge system along the western coast of Thailand (e.g. Jankaew et al. 2008; Gouramanis et al. 2017). Furthermore, although local beaches were lost in the 2004 tsunami, satellite photography showed rapid natural recovery within 18 months (e.g. Choowong et al. 2009).

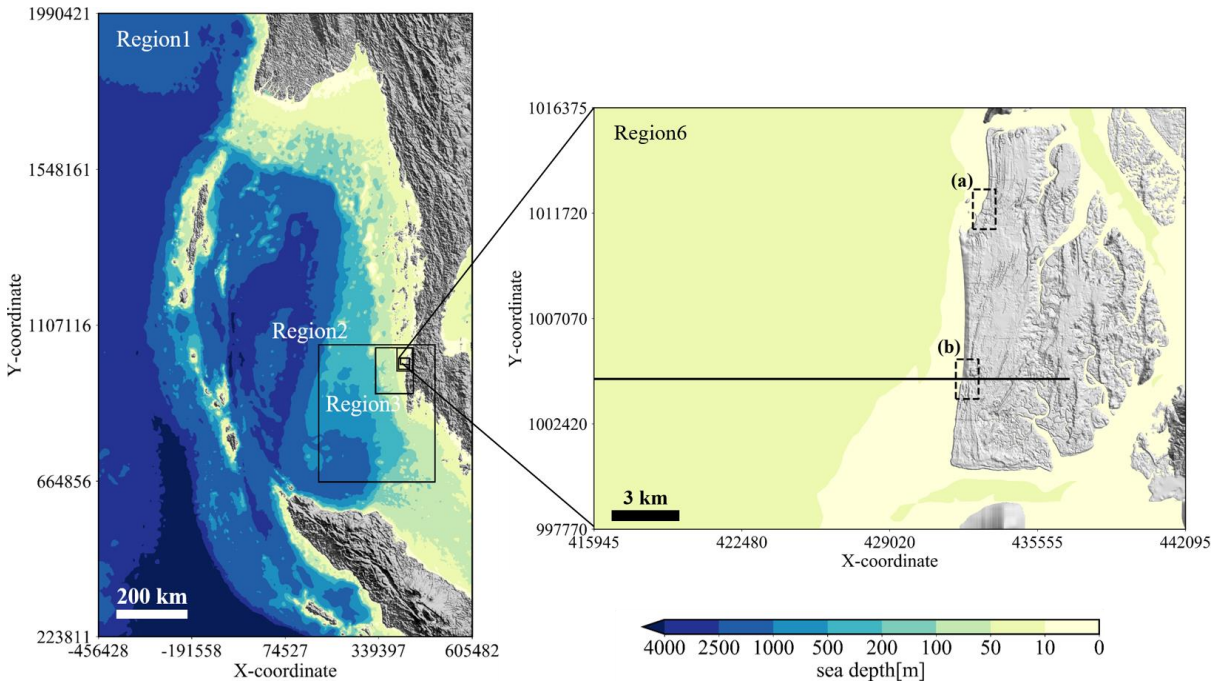

Figure 2 Terrain data (The black frame shows Region 1 to Region 6, and the black line in Region 6 shows the cross-section where calculation was performed. Dashed squares are the beach where erosion was confirmed from satellite image.)

2.2. *Topography and bathymetry data*

The topography and bathymetry data used for the tsunami sediment transport calculations were created based on various water depths and elevations. Figure 2 shows the terrain data that were created. Topographic data were downscaled from Region 1, which includes the Andaman Sea, to Region 6, which includes all of Phra Thong Island. The grid spacing decreases from Region 1 (the spatial grid size Δx_1= 1,215 m) to Region 6 (Δx_6= 5 m). In the tsunami sediment transport calculations, UTM zone 47N was used to geospatially constrain the horizontal modelling coordinates of Phra Thong Island. Region 1 is the projection of depth data of the 30-second grid provided by GEBCO (2014) on the Cartesian coordinate system UTM 47N. Regions 2–4 use a digital marine chart with 300 m resolution based on a survey by the Royal Thai Navy. Regions 5 and 6 use an original 5 m (terrain data) and 15 m (sea depth data) grid spacing to create mean terrain and water depth data based on analysis of satellite image by EOMAP and elevation data provided by the Land Development Department of Thailand (LDD, 2018). The terrain data of Region 4, created from the digital marine chart of 300 m resolution, showed discontinuity at the boundary with Region 5, which had a higher resolution. The discontinuity was therefore removed to the extent possible by interpolation with an inverse distance weighting method using all terrain data.

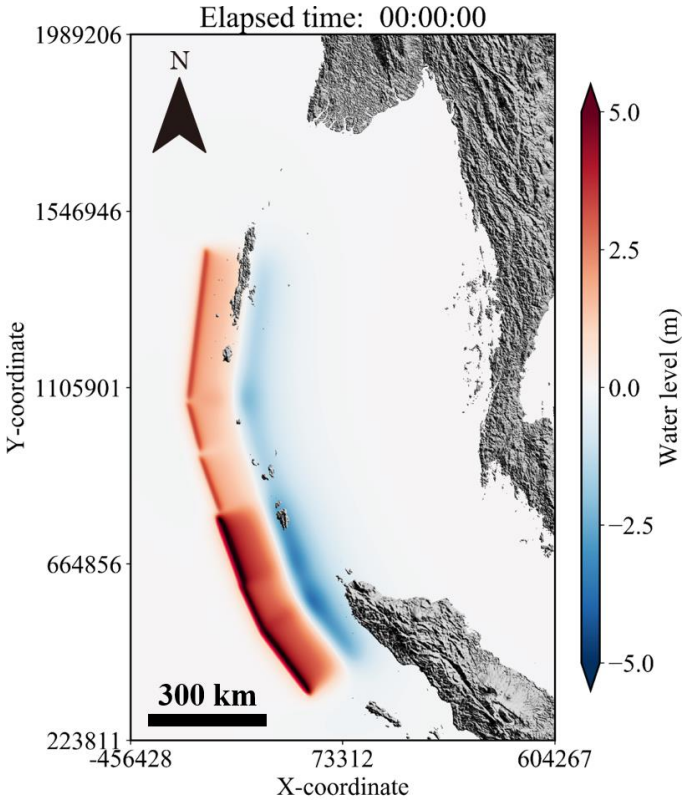

Figure 3 Initial water level after earthquake occurrence

Table 1 Earthquake fault parameters for calculating initial water level (Suppasri et al., 2011)

Segment No.	1	2	3	4	5	6
Latitude (°N)	3.03	4.48	5.51	7.14	8.47	9.63
Longitude (°E)	94.4	93.3	92.9	92.3	91.9	91.6
Strike (deg)	323	335	340	340	345	7.00
Dip (deg)	15.0	15.0	15.0	15.0	15.0	15.0
Slip (deg)	90.0	90.0	90.0	90.0	90.0	90.0
Length (km)	200	125	180	145	125	380
Width (km)	150	150	150	150	150	150
Dislocation (m)	14.0	12.6	15.1	7.00	7.00	7.00
Depth (km)	10.0	10.0	10.0	10.0	10.0	10.0

2.3. *Tsunami source model*

The tsunami source model proposed by Suppasri et al. (2011) was used as the tsunami source of the 2004 Indian Ocean Tsunami as the model focused on the coast of Thailand and accurately reproduced the inundation area and surveyed trace height of the 2004 IOT. The fault model is divided into six small faults from satellite image analysis and survey results, and it is assumed that each small fault slides simultaneously and instantaneously. For the tsunami source, the vertical tectonic displacement in each fault was calculated according to Okada (1985). Table 1 shows the fault parameters of each fault and

Figure 3 shows the initial water level.

2.4. *Tsunami sediment transport calculation*

2.4.1. *Tsunami propagation and run-up model*

Tohoku University's Numerical Analysis Model for Investigation of Near-field tsunamis, No. 2 (TUNAMI-N2) is based on the nonlinear long wave theory and was used as the tsunami propagation and run-up model (Imamura, 1996).

$$\frac{\partial \eta}{\partial t} + \frac{\partial M}{\partial x} + \frac{\partial N}{\partial y} = 0 \tag{1}$$

$$\frac{\partial M}{\partial t} + \frac{\partial}{\partial x}\left(\frac{M^2}{D}\right) + \frac{\partial}{\partial y}\left(\frac{MN}{D}\right) + gD\frac{\delta \eta}{\delta x} + \frac{gn^2}{D^{\frac{7}{3}}}M\sqrt{M^2+N^2} = 0 \tag{2}$$

$$\frac{\partial N}{\partial t} + \frac{\partial}{\partial x}\left(\frac{MN}{D}\right) + \frac{\partial}{\partial y}\left(\frac{N^2}{D}\right) + gD\frac{\delta \eta}{\delta y} + \frac{gn^2}{D^{\frac{7}{3}}}N\sqrt{M^2+N^2} = 0 \tag{3}$$

Here, η is the change in water level from the still-water surface, D is the total water depth from the bottom to the water surface, and g is the acceleration of gravity. The bottom friction is expressed according to the Manning formula, where n is Manning's roughness coefficient (n = 0.025). M and N are the total flow fluxes in the x and y directions, respectively, and are given by integrating the horizontal flow velocity u, v from the water bottom h to the water surface η. It is assumed that the horizontal flow velocity is uniformly distributed in the vertical direction.

The nonlinear long wave theory consists of a continuous equation that is derived from (1) the principle of conservation of mass (continuity equation) and (2) the conservation of momentum (equation of motion). These two equations are obtained by vertically integration from the seabed to the water surface.

When the water depth is about 50 m or less, the effects of the 2nd, 3rd and 5th terms of the advection and seabed friction terms (Equations 2 and 3) are reduced, therefore wave theory that omit these terms is often used at depths shallower than 50 m. Meanwhile, the Message Passing Interface (MPI) parallel was implemented in the model for highly efficient calculations. Both the advection term and the bottom friction term were therefore considered in the calculations without reducing accuracy in deeper waters.

The reproducibility of the calculated results is based on the tsunami height data (IUGG; available at http://www.nda.ac.jp/~fujima/TMD/index.html) for the 2004 IOT and is discussed using the geometric mean K and geometric standard deviation κ proposed by Aida (1978).

$$\log K = \frac{1}{n}\sum_{i=1}^{n} \log K_i \tag{4}$$

$$\log\kappa = \sqrt{\frac{1}{n}\left\{\sum_{i=1}^{n}(\log K_i)^2 - n(\log K)^2\right\}} \tag{5}$$

Here, n is the number of points, R_i is the tsunami height at the i^{th} point, H_i is the calculated value at the ith point, and $K_i = R_i/H_i$.

2.4.2. *Sediment transport model*

For the tsunami movable bed model, we used the numerical Sediment Transport Model (STM) proposed by Takahashi et al. (2000), which solves the time evolution of sediment transport considering the exchange sediment volume of the bed and suspended load layers according to the flow conditions of the nonlinear long wave theory-based TUNAMI-N2 model. For each time step in the finest calculation region (region 6), the STM receives the total flow fluxes from TUNAMI-N2 and calculates the change of seafloor and land surface and feeds this to the next time step of the TUNAMI-N2 model.

This model divides tsunami sediment transport into a bed load layer, where sediment grains pull, and a suspended load layer, where sediment grains float. The governing equations consist of continuous equations for the bed load layer and the suspended load layer:

$$\frac{\partial Z_{\mathrm{B}}}{\partial t} + \frac{1}{1-\lambda}\left(\frac{\partial q_{\mathrm{B},x}}{\partial x} + \frac{\partial q_{\mathrm{B},y}}{\partial y} + w_{\mathrm{ex}}\right) = 0 \tag{6}$$

$$\frac{\partial C h_{\mathrm{S}}}{\partial t} + \frac{\partial CM}{\partial x} + \frac{\partial CN}{\partial y} - w_{\mathrm{ex}} = 0 \tag{7}$$

Here, λ is the sediment grain porosity, Z_{B} is the bottom height from the reference plane, q_{B} is the amount of bed load sediment, C is the average suspended load layer concentration, h_{s} is the suspended load layer thickness (= total water depth), and M, N are the water discharges in the x direction and y direction, w_0 is the sedimentation velocity of the sediment grains.

Equation (6) is a continuous equation for within the bed load layer. The first term is the exchange sediment volume with the bottom, the second term is the balance of sediment flow volume moving in a tractive form in the flow direction, and the third term defines the balance of suspension flux, caused by diffusion, and sedimentation flux, caused by gravity, as the exchange sediment volume between the bed load layer and the suspended load layer.

Equation (7) is a continuous equation for within the suspended load layer. The first and second terms are bed load sediment moving in a suspended state in the flow direction, the third term is the exchange

sediment volume between the bed load layer and the suspended load layer, and the fourth term is the increase or decrease of the sediment flow in the suspended load layer.

In Equations (8) and (9), the equations defining the bed load sediment volume q_B and the equation defining the exchange sediment volume w_{ex} of the bed load layer and suspended load layer are necessary, but according to Takahashi et al. (2000), they are obtained by the following:

$$q_{B,x\,y} = \alpha\sqrt{sgd^3}(\tau_* - \tau_c)^{\frac{3}{2}} \tag{8}$$

$$w_{ex} = \beta\sqrt{sgd}(\tau_* - \tau_c)^2 - w_0 C \tag{9}$$

$$\tau_* = \frac{u_*^2}{sgd} \tag{10}$$

Here, α is the coefficient of the bed load sediment volume equation, β is the coefficient of the suspension volume equation, s is the submerged density of the sand particles ($s = \rho_s/\rho_w - 1$; ρ_s and ρ_w are the density of sand particles and water, respectively; $\rho_s = 2.65\ \mathrm{g/cm^3}$ and $\rho_w = 1.0\ \mathrm{g/cm^3}$), g is the acceleration of gravity, d is grain diameter, w_0 is the sedimentation velocity of the sediment grains, τ_* is the Shields number (Equation (10)), τ_c is the limit Shields number, $u_*$is the friction velocity obtained from the Manning formula ($u_*^2 = gn_s^2M|M|/D^{7/3}$). n_s is the roughness coefficient for STM. Note that the value of the roughness coefficient n used the tsunami calculation differs from n_s.

The grain-size dependent parameter for bed load (α) and exchange rate (β) in Equation (8) and (9) are derived from Equations (11) and (12) based on the hydraulic experiments by Takahashi et al. (2011):

$$\alpha = 9.8044e^{-3.366d} \tag{11}$$

$$\beta = 0.0002e^{-6.5362d} \tag{12}$$

However, the functions should not be applied when d is outside the 0.166 mm to 0.394 mm range as he validity of extrapolated d values may produce erroneous results.

$$w_0 = \sqrt{sgd}\left(\sqrt{\frac{2}{3} + \frac{36\nu^2}{sgd^3}} - \sqrt{\frac{36\nu^2}{sgd^3}}\right) \tag{13}$$

Equation (13) is a settling velocity of the sand particles by Rubey (1933). Here, ν is the kinematic viscosity coefficient ($\nu = 0.0139\ \mathrm{cm^2/s}$).

Considering the effect from the bed slope (Watanabe et al., 1984), the formulation of the bed load, q_B, Equation (6), is rewritten as Q_B as shown in Equations (14) and (15):

$$Q_{B,x} = q_{B,x} - |q_{B,x}|\varepsilon \frac{\partial Z_B}{\partial x} \quad (14)$$

$$Q_{B,y} = q_{B,y} - |q_{B,y}|\varepsilon \frac{\partial Z_B}{\partial y} \quad (15)$$

where ε is a diffusion coefficient of the sediments (ε = 2.5; Sugawara et al., 2014a).

Sediment transport during tsunami largely occurs as suspension (Takahashi et al., 2000). In such situations, suspended sediments are maintained in the water column by turbulence while the energy of the turbulence is dissipated due to the increased suspended sediment concentration. This induced an equilibrium state in which no further sediment supply from the bottom occurs. The resulting concentration is called the saturated sediment concentration. The expression for saturation concentration of suspended sediments C_s is applied as (Van Rijn, 2007; Sugawara et al., 2014a):

$$C_s = \frac{\rho_w}{\rho_s - \rho_w} \frac{e_s n_s^2 u^3}{h_s^{4/3} w_0 - e_s n_s^2 u^3} \quad (16)$$

where e_s is the efficiency coefficient (e_s = 0.025; Bagnold, 1966). Note that in the sediment transport calculation, the saturation concentration of suspend sediments given by Equation (16) is applied entrainment of sediment from the bottom layer. Namely, sediment supply from the bottom to the water column (suspended load layer) by w_{ex} is not permitted if $C \geq C_s$. However, supersaturation ($C \geq C_s$) due to sediment advection, or sudden decrease of C_s due to the change of flow parameters, is permitted. In this calculation, when C exceeds maximum concentration C_{max} was set to 0.377, based on the observed value (Xu, 1999a, 1999b).

In Equation (6) and Equation (7), the bottom height (Z_B) is determined from the reference plane, and the average suspended sediment concentration (C) are the initial values before the tsunami and the flow flux (M). Because suspended sediment thickness (h_s) is given by the equation of motion of a fluid and the continuous equation, sea level fluctuation can be determined over time. Further, the MPI parallel was implemented to enable relatively efficient wide area calculations (e.g. Yamashita et al. 2016).

2.5. *Calculation conditions*

The initial conditions for the numerical simulations used the terrain data (Figure 2) and tsunami source (Figure 3). The simulations were performed using a 3:1 nested grid that increased the resolution a 1215 m^2 grid to a 5 m^2 grid. Additionally, the target region of the sediment transport calculation was limited to Region 6, with a grid spacing of 5 m^2.

The simulations were calculated over a 0.05 second increment with a 6-hour period in which the test case with a 12 hour period showed the suspended sediment concentration in the vicinity of the shoreline

Table 2 Set parameters for sediment transport calculations

Parameter	Value
Coefficient of bed load sediment volume equation α	6.40
Coefficient of suspension sediment volume equation β	8.70×10^{-5}
Critical friction u_c	0.0137 m/s
Sedimentation velocity of sediment grains w_0	0.00971 m/s

decreased and stabilized. Therefore, 6-hour simulation was used for the reproduction of the 2004 tsunami as well as further sensitivity analysis of the grain size and roughness coefficient.

For the bottom conditions of STM, the roughness coefficient was fixed at n_s = 0.030 s/m$^{1/3}$, and the entire area of Region 6 was considered the movable bed. In general, when simulating tsunami sediment transport, it is necessary to determine the roughness coefficient according to land use. However, since there is no land use map before the tsunami on Phra Thong Island, a fixed value was used, similar to previous studies (e.g. Sugawara et al., 2014a, b; Yamashita et al., 2015; Yamashita et al., 2016). However, Sugawara et al. (2014a) showed that the variation in Manning's roughness coefficient for the sand beds may affect the general distribution pattern of sediment deposits and erosions across the artificial topographic features with much higher roughness coefficient such as artificial canals, roads and populated residential areas. Therefore, a sensitivity analysis on the roughness coefficient was performed. Phra Thong Island has no such artificial topographic features and using the single roughness coefficient should sufficiently capture the overall roughness. However, to ensure robust conclusions, a sensitivity analysis for two bottom conditions was performed at n_s = 0.025 s/m$^{1/3}$ and n_s = 0.035 s/m$^{1/3}$, which are within the range of previously used estimates of roughness (e.g. Sugawara et al., 2014a, b).

The grain size was based on one sediment data set (Gouramanis et al., 2017) from the locally eroded region, and was considered as a representative value for all of the tsunami sediment grain sizes. A uniform grain size of d = 0.127 mm was used. The critical Shields number τ_c in Equations (9) and (10) was obtained using Equations (17) and (18) according to Iwagaki et al. (1956):

$$\tau_c = u_c^2 \rho \tag{17}$$

$$u_c^2 = 8.41 d^{\frac{11}{32}} \tag{18}$$

Here, u_c is the critical friction and ρ is the density of water. Table 2 shows each parameter used for the sediment transport calculations in this study.

The numerical model used in this paper can only consider a single grain size, so the model cannot resolve the grading observed in the sand layers (e.g. Gouramanis et al., 2017). Additionally, initial bed grain size can have a large effect on erosion and deposition (e.g. Apotsos et al., 2011b; Sugawara et al., 2014a; Jaffe et al., 2016). Furthermore, the sediment data we used to set the grain size is from a single

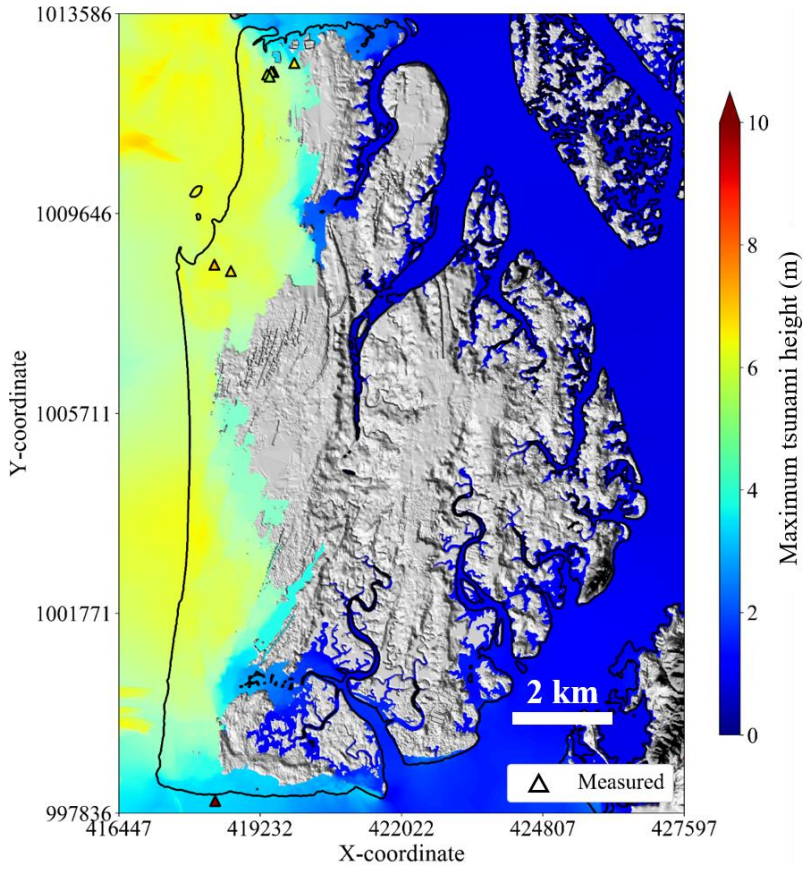

Figure 4 Comparison of calculated and measured maximum tsunami height

location in the north of the island, and is assumed to be a representative grain size for the tsunami deposits. As such we performed a sensitivity analysis on the grain size. Pham et al. (2018) investigated the surface grain size of the offshore (water depth > 15 m), nearshore (water depth < 15 m), and onshore on Phra Thong Island, which they considered to be the source of sediments that formed the tsunami deposits. Pham et al. (2018) recorded a mean grain size of 0.314 mm in the offshore area, 0.129 mm in the nearshore area, and 0.285 mm in the onshore area. Based on these mean grain sizes, we conducted a sensitivity analysis for two grain sizes (0.285 mm and 0.314 mm representing the offshore and onshore sediments)

3. Results

3.1. *Verification of reproducibility*

3.1.1. *Tsunami height*

Figure 4 shows the results of the calculation of the maximum tsunami heights and the seven measured tsunami heights on Phra Thong Island. From Equations (4) and (5), $K = 1.16$ and $\kappa = 1.4$ are obtained. The Japan Society of Civil Engineers (2012) consider $0.95 < K < 1.05$ and $\kappa < 1.45$ as guides for evaluating reproducibility of tsunami numerical calculations. Although the K value is slightly higher than the guideline but this is because of an uncertain 19.6 m measured in the southern part of the Island. Additionally, the source model used in this calculation gives $K = 0.84$ and $\kappa = 1.3$ for reproducibility of

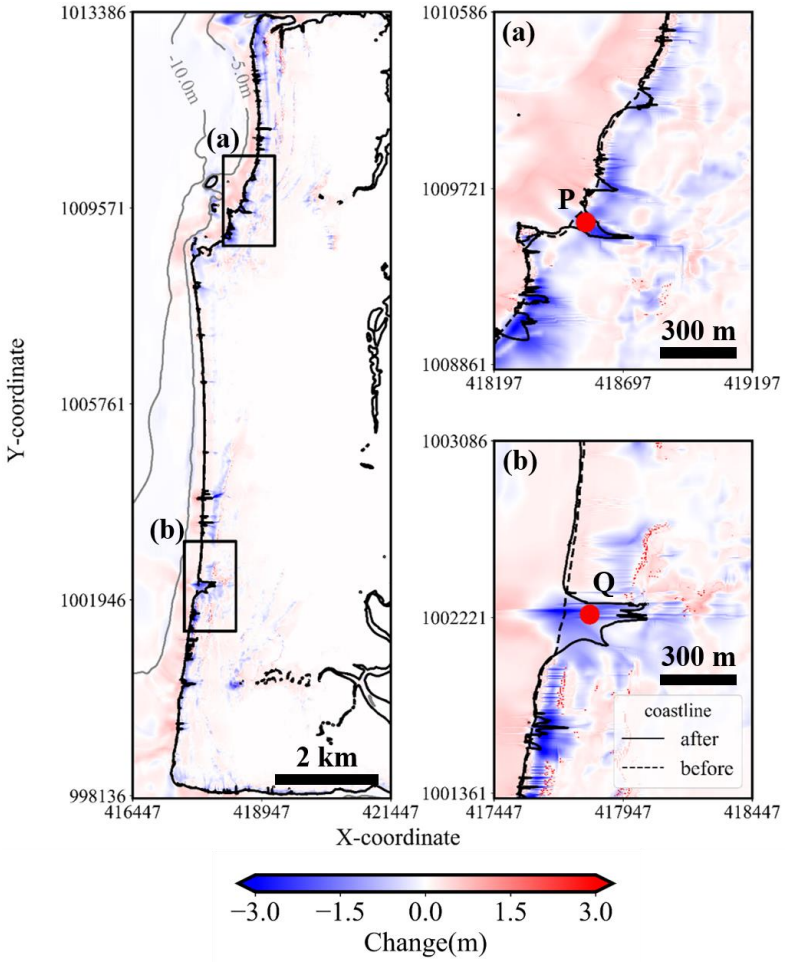

Figure 5 Topographic change and shoreline position caused by the tsunami (solid & dashed lines show that the coastline after and before the tsunami in the simulation, P and Q are the points confirmed local beach erosion in region (a) and (b), blue and red mapping show erosion and deposition after the tsunami in the simulation)

tsunami height in the wide area along the coast of Thailand (Suppasri et al., 2011). Therefore, it can be said that this calculation has the same tsunami reproducibility as the previous study.

3.1.2. *Shoreline changes*

Our sediment transport models identify the locations of significant sediment erosion, which are confirmed from post-tsunami satellite images. Figure 5 shows the pre-2004 IOT topographical and geomorphological features (dashed line) and the modelled changes caused by the tsunami (solid line). Erosion typically occurs locally where small tidal channels breach the youngest beach ridge system (Figure 5(a) and 5(b)). Comparison with the satellite image shows that the position of erosion in both regions is consistent (Figure 6). Although the actual amount of erosion is unknown, this indicates that the planar spread of the eroded component can be well reproduced by the calculation. Region (a) was further investigated in detail, as the area corresponds to the point where sediment outflow occurred (Jankaew et al., 2008).

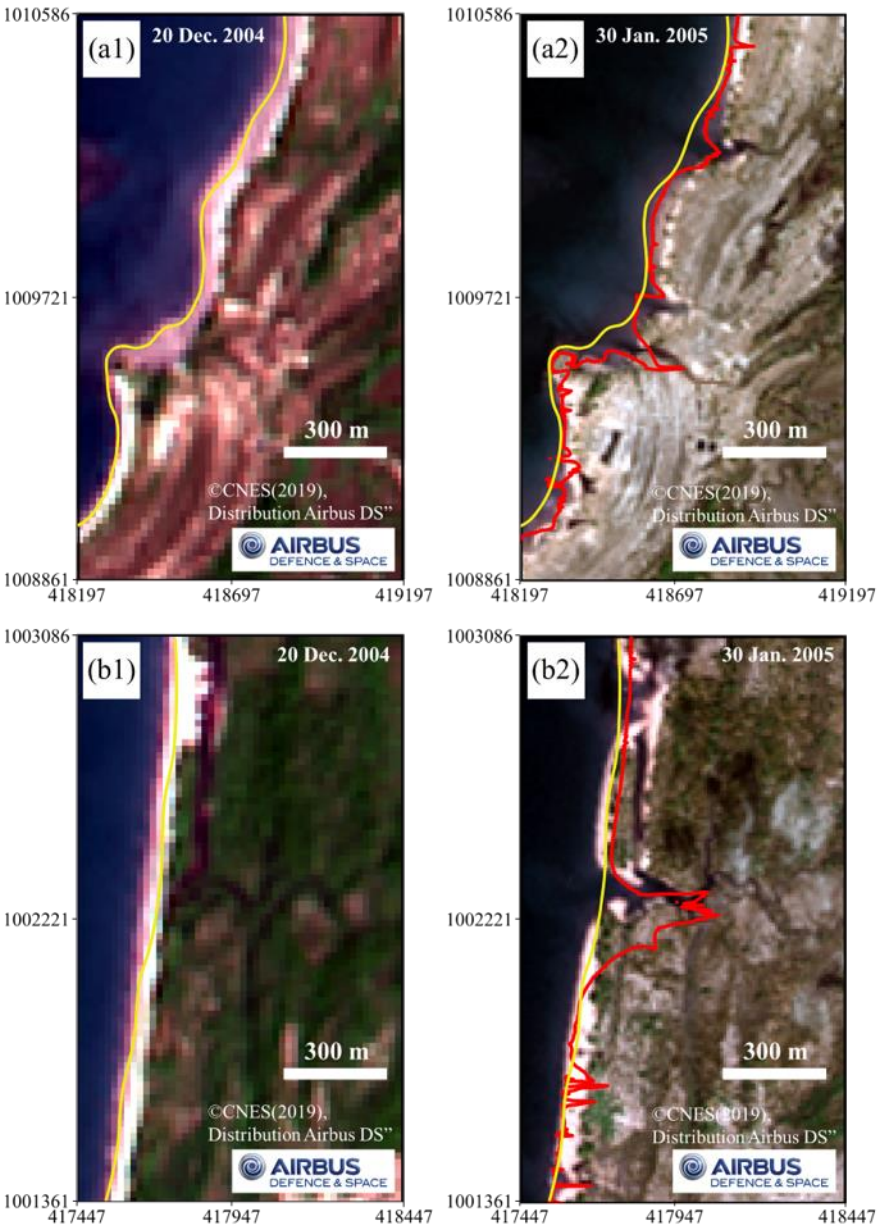

Figure 6 Comparison of observed shoreline position from Figure 5 region (a) and (b) derived from satellite images before and after the tsunami (20 Dec. 2004 and 30 Jan. 2005), which is overlain by the modelled extent of erosion showing that the modelled results closely match the observed changes. The red line is the calculated shoreline after the tsunami, and the yellow line is the shoreline before the tsunami (© CNES, 2019, Distribution Airbus DS"). a1) Satellite image before the tsunami in region (a), a2) Satellite image after the tsunami in region (a), b1) Satellite image before the tsunami in region (b), b2) Satellite image after the tsunami in region (b)

3.1.3. *2004 IOT onshore sediment deposition*

In addition to the erosional features, the model simulated the deposition of 2004 IOT sediments across the island. The thickness of these simulated deposits are compared with 133 measured 2004 IOT deposit

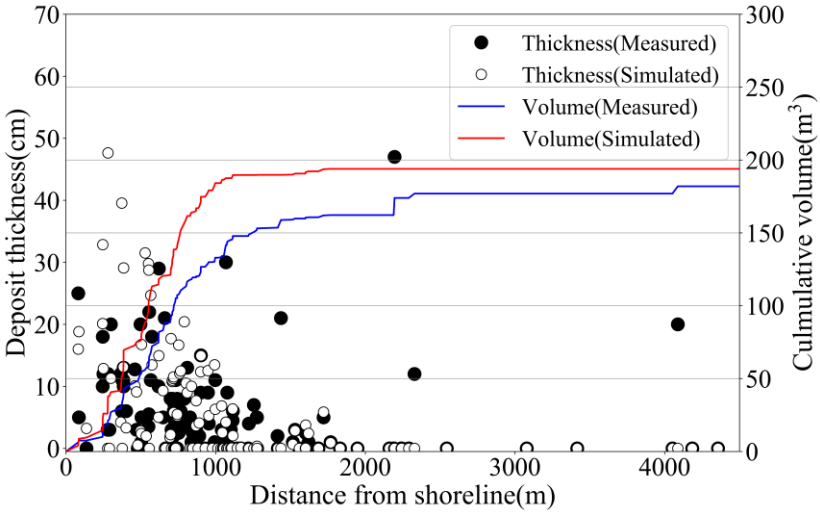

Figure 7 Comparison of field measured and simulated tsunami deposit thickness using a representative grain size of d = 0.127 mm. Black point shows the measured thickness by Jankaew et al. (2008) and Gouramanis et al. (2017), white point shows the simulated thickness. Blue and red line show the cumulative curves of measured data and simulated data.

thicknesses (Jankaew et al., 2008; Gouramanis et al., 2017). Figure 7 shows a comparison of layer thicknesses at each site (black circles for measured results and white circles for simulated results), which shows that most of the sites are overestimated within 1 km from the shoreline and underestimated at distances greater than 2 km from the shoreline. The model specification and topographical data can be considered as the major causes of this error.

First, considering the overestimation within 1 km of the inundation distance, it is found that the STM has a setting of the maximum suspended concentration, C_{max} as 37.7% (Xu, 1999a and 1999b). The computed suspended concentration in this area is higher than C_{max}. Therefore, the surplus sediment is forced to be deposited in this zone causing overestimation. Pham et al. (2018) found that the source of tsunami deposits in Phra Thong Island is mainly the sediment from the nearshore zone. In other words, the first wave, which had the highest wave height, eroded a large amount of sediment in the nearshore and transported a large amount of sediment inland. Therefore, it is considered that the maximum concentration was reached during the first wave run-up because of the very high concentration of suspended sediment, which led to the overestimation of the forced sedimentation in the simulation.

Second, considering the underestimation of the deposition in inundation distances of 2 km or more, the most likely reason is the computational grid and the model specification. Previous studies have shown that tsunami deposits are highly affected by locality features (e.g. Sugawara et al., 2014a; Watanabe et al., 2018). As shown in three locations with the actual measured deposit thickness (dashed boxes) in Fig. 8, it can be seen that most of the measured thickness is zero which indicate and support the reasons of localized deposition. Although the computational grid is very fine (Δx_6= 5 m), it is difficult to reproduce local sedimentation with averaged elevation data. In addition, this STM uses only a single grain size and can only model deposits consisting of sand grain-sizes. Sugawara et al. (2014a)

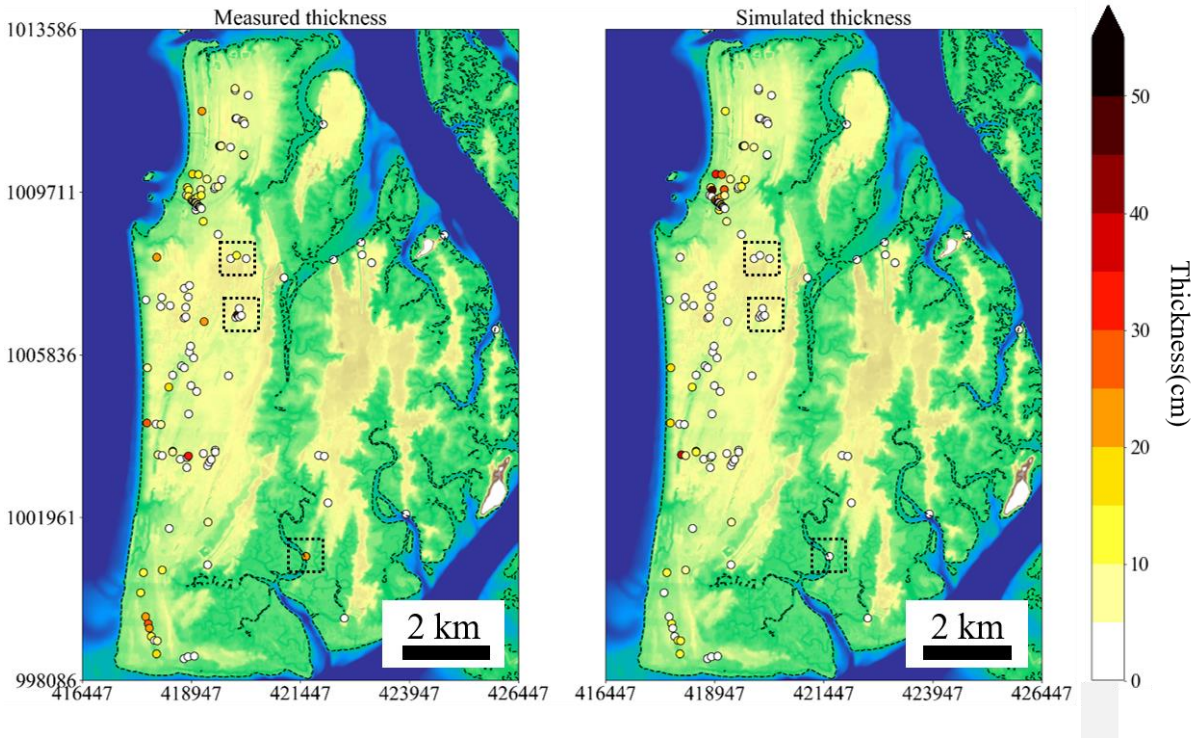

Figure 8 Spatial distribution of measured and simulated thickness of tsunami deposits. The black dotted lines indicate that the calculated values are underestimated at distances greater than 2 km.

conducted tsunami sediment transport simulation on the Sendai Plain and discussed the transportation possibility of finer grained sandy and muddy sediment. Muddy sediments were also found in the Sendai Plain at a distance of 2 km or more from the 2011 tsunami. Sugawara et al. (2014a)'s STM-based tsunami sediment transport simulation could not be reproduced for Phra Thong Island, also due sandy sediment and a single grain size model limitations. Therefore, it is possible that muddy or very fine-grained sediment was deposited at the three sites but were underestimated in the simulations using the current model.

Based on all above-mentioned reasons, it is more practical to evaluate the simulation results by the overall trend of the tsunami deposit rather than comparing the thickness point by point. In Figure 7, the line of "Cumulative volume" show the cumulative deposition expressed at each point by the sediment thickness multiplied by the area of the computational grid. In general, the tsunami deposits are greatly affected by local micro-topography (Sugawara et al., 2014a; Jaffe et al., 2016), and it is difficult to fit the modelled layer thickness with the observed layer thickness using DEM averaged in a computational grid. Therefore, we introduce the concept of cumulative sedimentation, and evaluated the scale of the amount of sediment movement generated. Although the modelled layer thickness typically overestimates the observed layer thickness by +7%, such low variation suggests a relatively successful reproduction of the observed dataset (Figure 7). The modelled overestimation is likely due to the assumption that the entire exposed land area would act as a movable bed. In reality, this is an oversimplification of the true ground surface, which contains vegetation that binds and traps the soil

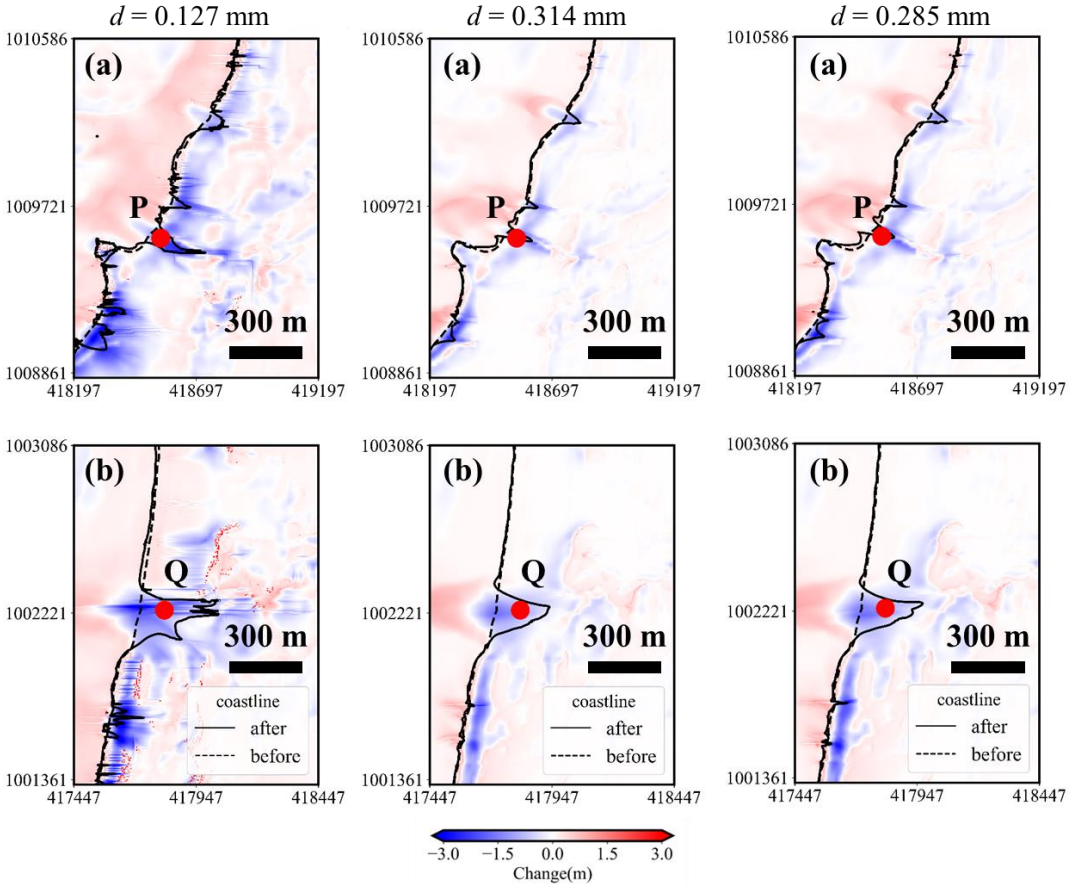

Figure 9 Topographic change and shoreline position caused by the tsunami for each grain size

Table 3 volume of erosion and deposition in regions (a) and (b) for each grain size (Percentage shows the ratio to reference)

	d (mm)	Erosion (m^3)		Deposition (m^3)	
		Region (a)	Region (b)	Region (a)	Region (b)
Reference	0.127	352,333	314,189	259,379	254,417
Onshore	0.285	143,793 (41%)	155,225 (49%)	161,810 (62%)	149,470 (59%)
Offshore	0.314	117,491 (33%)	128,289 (41%)	137,749 (53%)	128,801 (51%)

and wet regions (i.e. in swales) that would have higher degrees of sediment cohesion, reducing the area that would be eroded. In addition, the model also reproduces the inland thinning of the 2004 IOT deposit. Based on these results, comparison of the sediment layer thickness of the 2004 tsunami shows that the scale and the overall sediment transport trend are comparable, and therefore, the results are sufficiently reproducible with confidence to evaluate the actual sediment transport.

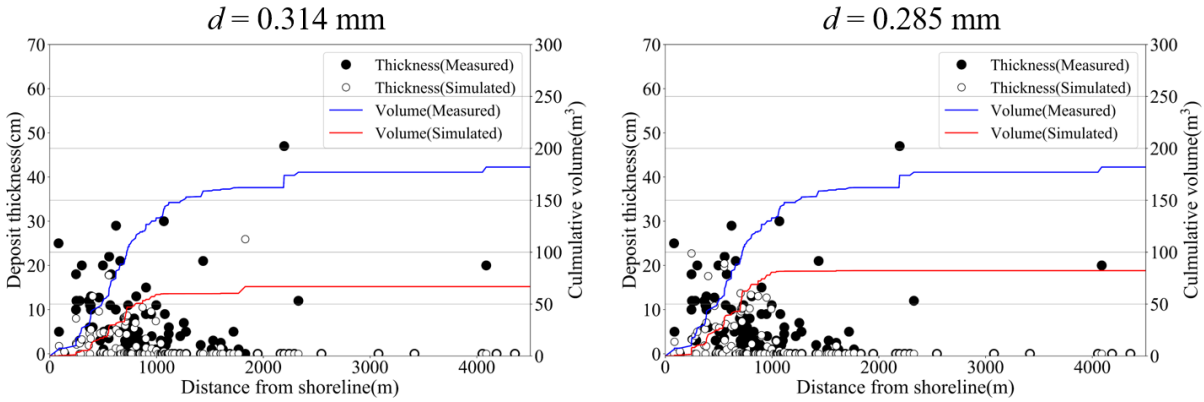

Figure 10 Comparison of field measured and simulated tsunami deposit thickness for each grain size.

3.1.4. *Sensitivity analysis for grain size and roughness*

Figure 9 shows the topographical changes and the thickness of the sediment layers used in this calculation for each grain size, and Table 3 shows the volume of erosion and deposition in regions (a) and (b). These figures show that smaller the particle size is, the greater the topographic change. This can be understood by the smaller the particle size, the larger the Shields number in Eq. (10), which indicates the ease of sediment transport, and the greater the amount of bed load in Eq. (8). However, Figure 9 suggests that the qualitative characteristics of sediment transport are the same in the three cases, due to the local erosion position of the beach in region (a) and (b) did not change for any particle size. And then, comparing the tsunami sediment thickness in Figure 10 the errors of the cumulative volume of d = 0.314 mm and d = 0.285 mm are -63% and -55%. Therefore, the grain size of d = 0.127 mm is considered to show the better reproducibility.

Figure 11 shows the topographical changes and thickness of sediment layer in this calculation for each bottom roughness coefficient, and Table 4 shows the volume of erosion and deposition in regions (a) and (b). These figures show that larger the value of roughness coefficient n_s is, the greater the topographic change. This can be understood by larger the roughness, the larger the Shields number in Eq. (10) because the friction velocity is proportionate to n_s. Therefore, an increase in the roughness coefficient indicates the ease of sediment transport, and the greater the amount of bed load in Eq. (8). However, Figure 11 suggests that the qualitative characteristics of sediment transport are the same in the three cases, due to the local erosion position of the beach in region (a) and (b) did not change for any bottom conditions. And then, comparing the tsunami sediment thickness in Figure 12, the errors of the cumulative volume of n_s= 0.025 s/m$^{1/3}$ and n_s= 0.035 s/m$^{1/3}$ are -8% and 13%. Therefore, the roughness coefficient of n_s= 0.030 s/m$^{1/3}$ is considered to show the better reproducibility.

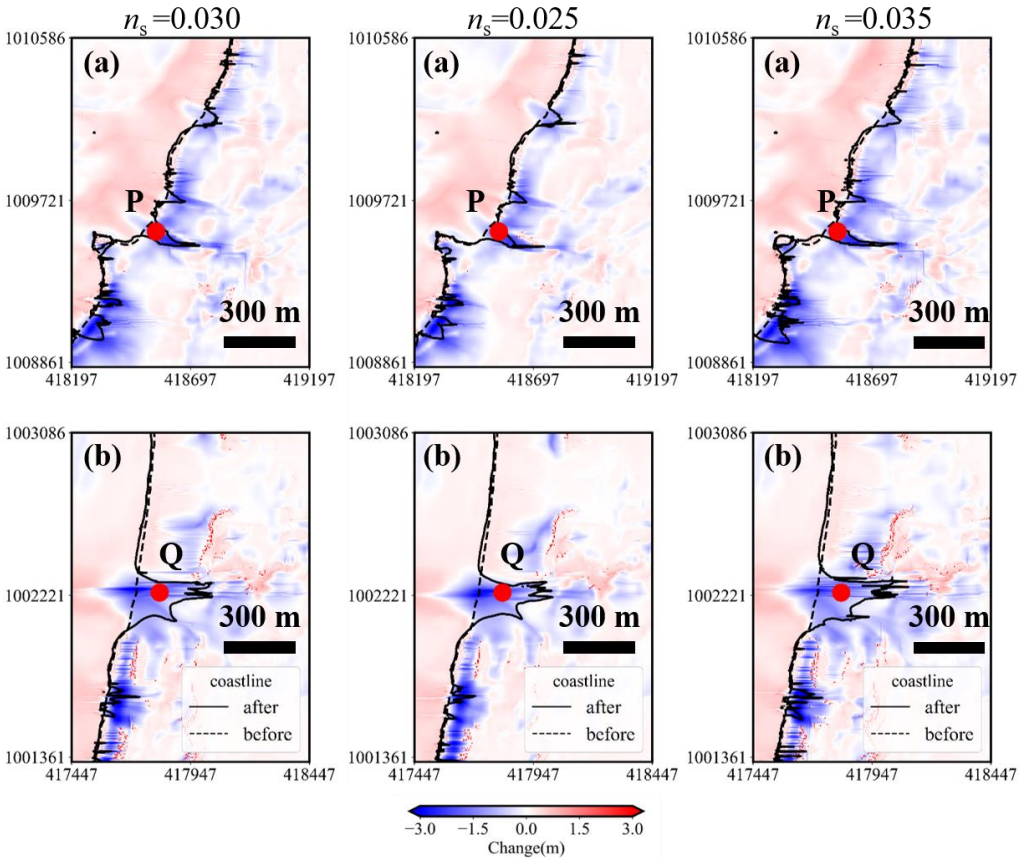

Figure 11 Topographic change and shoreline position caused by the tsunami for each roughness coefficient

Table 4 volume of erosion and deposition in regions (a) and (b) for each roughness coefficient (Percentage shows the ratio to reference)

	n_s (s/m$^{1/3}$)	Erosion (m^3)		Deposition (m^3)	
		Region (a)	Region (b)	Region (a)	Region (b)
Reference	0.030	352,333	314,189	259,379	254,417
Low	0.025	293,032 (83%)	285,659 (91%)	249,242 (96%)	230,905 (91%)
High	0.035	410,323 (116%)	352,284 (112%)	272,394 (105%)	262,522 (103%)

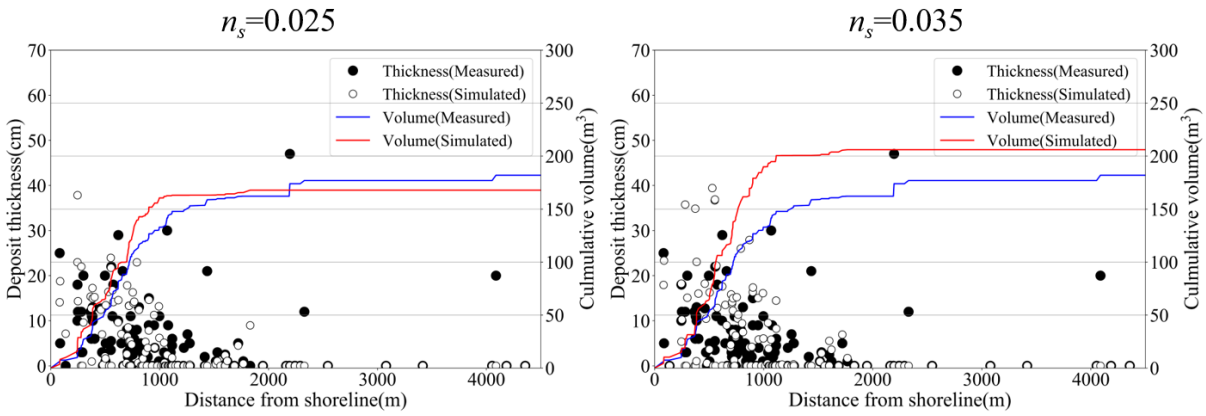

Figure 12 Comparison of field measured and simulated tsunami deposit thickness for each roughness coefficient.

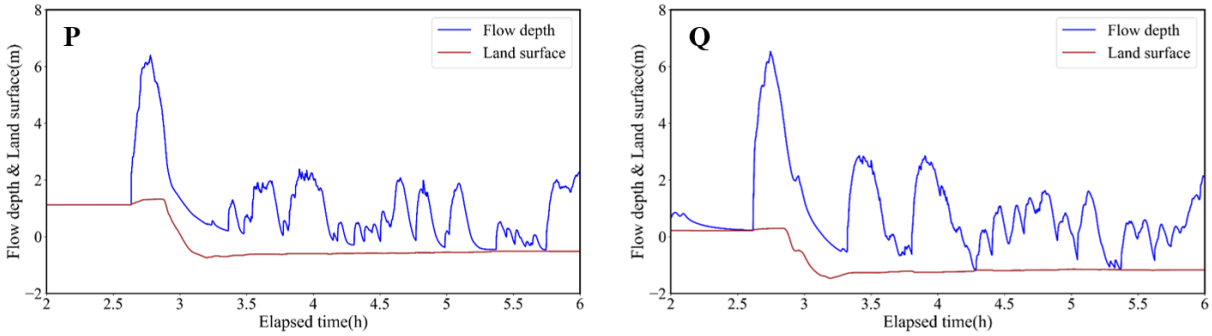

Figure 13 Chronological change of flow depth and land surface at point P and Q in region (a) and (b) (blue line shows the flow depth and red line shows the land surface)

3.2. *Sediment transport process*

Although the model reproduces the zones of sediment erosion and deposition well, the sediment transport processes during the tsunami event are further examined in regions (a) and (b) in Figure 5. The modelled time series of the changes of water height and elevation at point P in region (a) and point Q in region (b) are shown in Figure 13. The modelling results show that the first wave arrived 2 hours40 minutes after the earthquake, and backwash was generated 10 minutes later (Figure 13). In addition, the ground surface elevation increased by about 30 cm through sediment deposition during the first inflowing wave and more than 1.5 m was eroded during the backwash transporting sediment towards the ocean, so beach loss in both regions is considered to be a result of erosion during the backwash (red line in Figure 13).

In addition, no major topographic changes occurred on the beaches in both areas after the second wave backwashed, most of the sediment movement on the eroded beaches is considered to have been completed by the second wave drawback. In other words, the sediment transport processes during this period are the most important to examine the shoreline changes that occurred during the tsunami and set up the primary conditions for beach recovery post-tsunami. As such, there are two narrow time periods that highlight the key factors that for establishing the initial conditions of the recovery process.

First, why was not the beach eroded by the inflowing waves? Second, how did the sediment flowing seaward in the first wave move?

Based on the waveform (which assumes a flat surface), a shore-normal cross section calculation was carried out along the transect in Figure 2. The transect covers the region (b) from 1000 m offshore across the shoreline and 1000 m inland. Beyond these distances the planar effect was considered to be negligible. Figure 14 shows the changes in ground level, water level, suspended sediment concentration and saturation of suspended sediment concentration on the transect at each unit of time as waves washed in and out.

3.2.1 *Why was not the beach eroded by the pushing wave?*

As shown in Figure 14, prior to the first wave, the ocean receded to below approximately 8 m below mean sea level. As inflow of the first wave began, sediment was eroded from the sea floor at *ca*. 5-10m below mean sea level. This nearshore erosion increased the suspended sediment concentration as the first wave propagated onshore. At the shoreline, the suspended sediment concentration saturated and sedimentation could begin at the shoreline. In other words, it is estimated that sediment eroded the nearshore (5 m < depth < 10 m) environment during the first inflowing wave, and much of this sediment was transported shoreline and inland.

It should be noted that, there will be no increase in suspended sediment when the suspended sediment is saturated in the model and is the likely reason that the beach was not eroded by the inflowing first wave. Although there is a possibility that the beach was actually eroded, the numerical results suggest that the erosion in shallow coastal waters (deeper than 5 m but shallower than 10 m) resulted in a very high concentration of suspended sediment when the inflowing first wave entered -5 m to the beach section of the coast and sediment ceased to be entrained. Pham et al. (2018) found that the source of the 2004 IOT deposits on Phra Thong Island was from the nearshore (depth < 15m). This means that large scale erosion in shallow water has occurred and a large amount of sediment has been transported inland which agrees with the simulation results. Therefore, it is highly likely that the sediment concentration was very high when it reached the beach during the 1st inflowing wave. Takahashi (2012) showed that when the suspended sediment is in a high concentration state, turbulence is suppressed and the ability to retain suspended sediment may decrease. Therefore, it is highly probable that the same phenomenon occurred on Phra Thong Island and the beach erosion during the inflowing wave was suppressed.

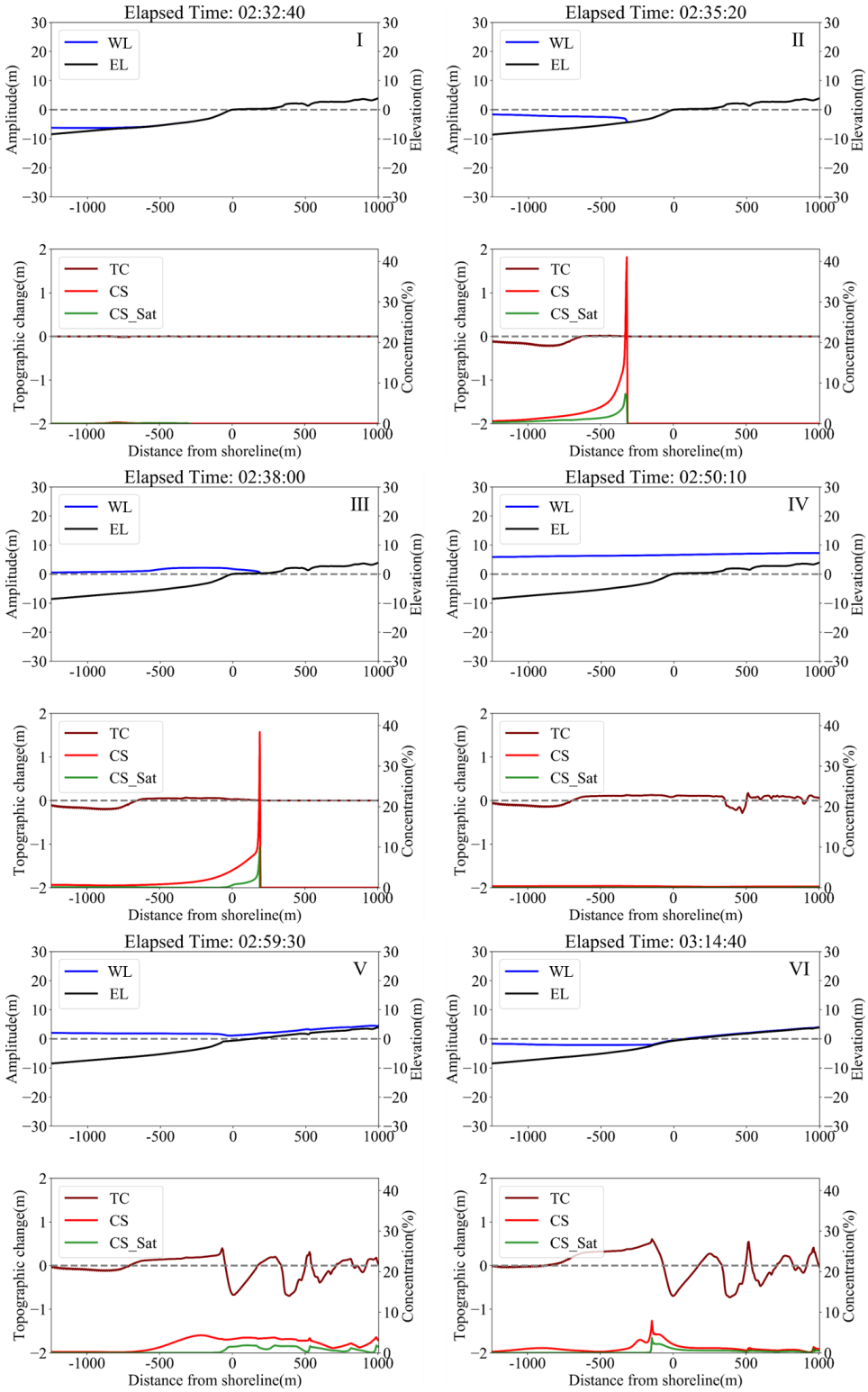

Figure 14 Change in water level (WL), land surface (EL), topographic change (TC), suspended sediment concentration (CS), and saturation suspended sediment concentration (CS_Sat) by section calculation along the survey line in region (b). (I) before the 1st inflowing wave, (II) Advance of 1st leading wave in shallow water, (III) Start of 1st leading wave run-up, (IV) Maximum of 1st leading wave , (V) Advance of 2nd backwash, (VI) Maximum of 2nd backwash

3.2.2 *How did the sediment flowing seaward in the first wave move?*

In Figure 14, at the initiation of backwash, the suspended sediment concentration is low. As backwash flows towards the ocean, the velocity increases, which increases erosion and causes the suspended sediment concentration to increase. This finding is consistent with the changes recorded in Figure 13. Beach erosion due to backwash has also been confirmed in for the 2004 IOT in Sri Lanka and the 2011 Tsunami along the Sendai Plain and at Rikuzentakata. (e.g. Tanaka et al., 2007, Tanaka et al. 2011, Yamashita et al. 2015, 2016). On the Sendai Plain, the estuary section of the old river tends to increase the return flow due to the tsunami (Tanaka et al., 2007, Tanaka et al. 2011). Therefore, there is a possibility that the region (a) and (b) (Fig. 2, 5 and 6) where local beach erosion of the backwash occurred on Phra Thong Island are the old river part.

Conversely, the entire beach was eroded by the return flow in Rikuzentakata (Yamashita et al., 2015, 2016), but no erosion was observed along the entire beach on Phra Thong Island and the Sendai Plain. Yamashita et al. (2015, 2016) suggested that the difference between Rikuzentakata and the Sendai Plain may be related to the horizontal distance of the plains. On the Sendai Plain, the inland topographic gradient is small, the inundation distance is long and the inland inundation depth tends to be small. Therefore, the potential energy that the inundation depth changes to kinetic energy during the backwash (return flow) becomes relatively small. The Sendai Plain and Phra Thong Island are flooded plains over 2 km inland and have similar topographical features.

From the above reasons, the local beach erosion due to the return flow on Phra Thong Island occurred at the mouths of tidal channels and within tidal channels and that minimal erosion occurred across the wider beach ridge strand plain. As backwash of the first wave ended, the water still contained a high suspended sediment concentration and this was deposited in the nearshore environment at less than 5 m water depth (Figure 15). After that, no significant topographic change was found. Thus, this modelling shows that most of the sediment that eroded from the onshore area was deposited in the shallow nearshore zone.

4. Discussion

4.1. *Sediment transport process and beach erosion*

Regions (a) and (b) were selected for detailed investigation of the simulation results and discussed. On Phra Thong Island, the 2004 IOT wave was large enough to expose the nearshore sediments and entrained most of its sediments from the shallow offshore region (below 5m). The wave ran up the exposed nearshore area while retaining sediment from the shallow offshore region. The sediment concentration gradually increases as the wave runs up the relatively long distance of the exposed nearshore zone, and became sediment-saturated as the wave reached the shoreline, making it difficult for new sediment to be eroded further. This explains why there was little erosion of the beach during the inflowing wave, and may be a characteristic sediment transport properties of shallow beaches like those on Phra Thong Island. The numerical simulation results suggest that there is little transportation

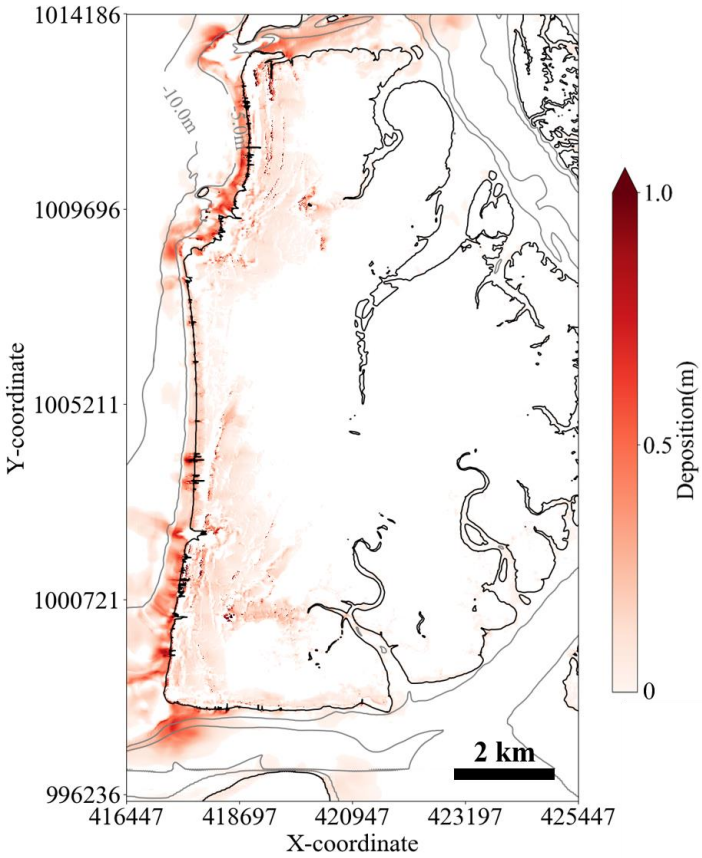

Figure 15 Sediment distribution derived from the simulation (showing depth contours at 5 m intervals in the sea area)

of sediments from beach by the first inflowing wave and that inland tsunami deposits originated from the nearshore environment. This finding validates Sawai et al. (2009)'s observation that the 2004 IOT entrained diatoms from shallow offshore waters at Phra Thong Island, and Pham et al. (2018)'s observation that sediment grain sizes and mineralogy were most similar to those of nearshore sediments. Figure 15 shows the results of the calculated sediment deposition both onshore and offshore Phra Thong Island. From the modelling results, most of the eroded sediment was deposited in shallow nearshore environments in water less than approximately 5 m deep.

The simulations show that the eroded sediments were deposited in the nearshore zone during backwash (Fig. 15), which primed the coastal zone for rapid coastal recovery. The removal of sediment from the onshore coastal zone also generated accommodation space that may have contributed to the coastal recovery process. Future studies can build on these findings to determine the extent of sediment transport and deposition, and identify the processes of coastal recovery on Phra Thong Island.

Geomorphologically, the Sendai Plain, which was inundated by the March 11, 2011 Great East Japan tsunami, is similar to the beach ridge plain on Phra Thong Island (Tanaka et al., 2011), but most of the tsunami sediment deposited onshore came from terrestrial sources (Goto et al., 2012; Szczucin´ski et al., 2012; Takashimizu et al., 2012; Sugawara et al., 2014b). However, the Great East Japan tsunami differed from the 2004 IOT as the Japanese event had a much smaller receding wave (Nationwide Ocean

603 Wave information network for Ports and HArbourS, NOWPHAS). As such the Japanese tsunami may
604 not have achieved sediment saturation as the wave approached the shoreline, thereby containing a lower
605 sediment concentration and allowing large volumes of sediment to be entrained from the beach for
606 subsequent formation of inland deposits. The different sources of deposited sediment in the two areas
607 reflects contrasting sediment transport mechanisms on shallow beaches, and may be useful for
608 identifying paleotsunami from coastal recovery and geological records.
609
610 **4.2.** ***Limits of calculation results***
611 This study analyzed tsunami sediment transport on Phra Thong Island using numerical calculations
612 and assumed that the island was unvegetated and lacked topography. However, the western half of the
613 island has an undulating surface caused by the beach ridge and swale system, and is extensively
614 vegetated with trees and dense grasses on the ridges and thick grasses within the swales. The eastern
615 half of the island has wide tidal channels and an extensive fringing mangrove system. Both topography
616 and differing vegetation types add complexity to the inundation and backflow sediment transport
617 models not captured here. In future, it is necessary to consider the influence of vegetation on tsunami
618 sediment transport.
619 Another potential limitation of the model is the selection of a single (median) grain size for the
620 sediments. As shown in previous studies (e.g. Sugawara et al., 2014a, b), the assumption of transport of
621 single grain sized sediment differs from actual situations because of the distribution of grain sizes
622 mobilised and deposited by tsunami. Therefore, it is important to set representative grain sizes and fully
623 study how grain size affects tsunami sediment transport. Future modelling may consider simulating the
624 suite of grain sizes individually or simulating a population of grain sizes that are identified in the modern
625 environment and in preserved tsunami deposits.
626 Furthermore, although the calculation was performed considering the entire area a movable bed, the
627 existence of fixed beds, such as rocky areas, should be considered. We consider this a minor component
628 of this research as the rocky headlands that serve as fixed beds are relatively small in area and would
629 contribute little to the overall simulations in our models.
630 Sugawara et al. (2014b) considers the simulation result of sediment layer thickness using the tsunami
631 sediment transport calculation to be affected by grain size, bottom conditions and topographic data.
632 Their study showed that the layer thickness increases as grain size becomes finer and the layer thickness
633 distribution tendency was unchanged regardless of grain size. Similar results were obtained in this study.
634
635
636 **5. Conclusion**
637 Because of insufficient knowledge about the topographic recovery process after a tsunami, this study
638 used sediment transport modelling to identify the erosional and depositional processes affecting the
639 coastal zone at Phra Thong Island, Thailand during the 2004 Indian Ocean Tsunami.
640 First, it was confirmed by comparing simulated results of the shoreline and sediment layer thickness

that the location of beach runoff identified on Phra Thong Island was reproducible and consistent with sediment transport results (Figs. 6 and 7). Based on the sediment transport results we conclude that the processes of sediment erosion and deposition on Phra Thong Island are characterized by the following sequence:

- erosion caused by the inflowing waves occurred at a relatively shallow location in the offshore area and the transported sediment was deposited near the shoreline;
- the inflowing waves caused minimal erosion of the shoreline; and,
- erosion of the shoreline was largely caused by backwash resulting in onshore sediments deposited in the shallow nearshore zone.

These erosional and depositional processes demonstrate the locations of sediment removal and subsequent deposition during the different phases of the first tsunami wave on Phra Thong Island which will serve as an important baseline of sediment sources for further study of the recovery process. The simulations also show that the zones of erosion and deposition across the island and offshore coastal zone are non-uniform. In particular, the zones of erosion and deposition highlighted in the simulations establish the environmental conditions that existed in the transitional phase between catastrophic tsunami and normal coastal processes that facilitated coastal recovery.

6. Acknowledgements

We would like to express our gratitude for the support from Dr. Panon Latcharote of the Faculty of Science and Technology of Thammasat University, Prof. Supot Teachavorasinskun, Dean of Faculty of Engineering, Chulalongkorn University, Dr. Pitcha Jongvivatsakul, Department of Civil Engineering Chulalongkorn University; and data from the Royal Thai Navy. RM, AS, KY, FI was support by JSPS Grant-in-Aid for Scientific Research (A) No. 17H01631 (FY2017 - FY2021). AS and NL was support by JSPS Bilateral program for joint research with National Research Council of Thailand (NRCT) (FY2017 - FY2018). CG was supported by NUS grant (R-109-000-223-133). NL was supported by Ratchadapisek Sompoch Endowment Fund (2019), Chulalongkorn University (762003-CC). This work is a contribution to IGCP Project 639, 'Sea-level Change from Minutes to Millennia'.

References

1) Abe, T., Goto, K., and Sugawara, D.: Relationship between the maximum extent of tsunami sand and the inundation limit of the 2011 Tohoku–oki tsunami on the Sendai Plain, Japan, Sedimentary Geology, 282, 142–150, 2012.
2) Aida, I.: Reliability of a tsunami source model derived from fault parameters, J. Phys. Earth, 26, 57–73, 1978.
3) Ali, P. Y., and Narayana, A. C.: Short-term morphological and shoreline changes at Trinkat Island, Andaman and Nicobar, India, after the 2004 tsunami. Marine Geodesy, 38(1), 26-39, 2015.
4) Arimitsu, T., Kawasaki, K., and Nimura, M.: Numerical simulation of sediment transport and

679 bottom topography change due to tsunami with large scale eddy, Journal of JSCE, B2 (Coastal
680 Engineering), 73, 2, 643–648, 2012.
681 5) Apotsos, A., Buckley, M., Gelfenbaum, G., Jaffe, B., and Vatvani, D.: Nearshore tsunami
682 inundation model validation: toward sediment transport applications. Pure and Applied
683 Geophysics, 168, 2097-2119, 2011a.
684 6) Apotsos, A., Gelfenbaum, G., and Jaffe, B.: Process-based modeling of tsunami inundation
685 and sediment transport, Journal of Geophysical Research, 116, F01006, 2011b.
686 7) Apotsos, A., Gelfenbaum, G., Jaffe, B., Watt, S., Peck, B., Buckley, M., and Stevens, A.: Tsunami
687 inundation and sediment transport in a sediment-limited embayment on American Samoa: Earth-
688 Science Reviews, 107, 1-11, 2011c.
689 8) Bagnold, R. A.: An approach to the sediment transport problem from general physics. US
690 government printing office, 1966.
691 9) Brill, D., Klasen, N., Jankaew, K., Brückner, H., Kelletat, D., Scheffers, A., and Scheffers, S.: Local
692 inundation distances and regional tsunami recurrence in the Indian Ocean inferred from
693 liminescence dating of sandy deposits in Thailand, Natural Hazards and Earth System Sciences,
694 12, 2177–2192, 2012a.
695 10) Brill, D., Klasen, Brückner, H., Jankaew, K., Scheffers, A., Kelletat, D., and Scheffers, S.: OSL
696 dating of tsunami deposits from Phra Thong Island, Thailand, Quaternary Geochronology, 10, 224–
697 229, 2012b.
698 11) Brill, D., Jankaew, K., Bruckner, H.: Holocene evolution of Phra Thong's beach-ridge plain
699 (Thailand) — Chronology, processes and driving factors, Geomorphology, 245, 117–134, 2015.
700 12) ChaguéGoff, C., Andrew, A., Szczuciński, W., Goff, J., and Nishimuira, Y.: Geochemical
701 signatures up to the maximam inundation of the 2011 Tohoku–oki tsunami — Implications for the
702 869 AD Jogan and other palaeotsunamis, Sedimentary Geology, 282, 65–77, 2012.
703 13) Choowong, M., Phantuwongraj, S., Charoentitirat, T., Chutakositkanon, V., Yumuang S., and
704 Charusiri, P.: Beach recovery after 2004 Indian Ocean tsunami from Phang–nga, Thailand,
705 Geomorphology, 104, 134–142, 2009.
706 14) Fagherazzi, S. and Du, X.: Tsunamigenic incisions produced by the December 2004 earthquake
707 along the coasts of Thailand, Indonesia and Sri Lanka, Geomorphology, 99, 120–129, 2008.
708 15) Feldens, P., Schwarzer, K., Szczuciński, W., Stattegger, K., Sakuna, D. and Somgpongchaiykul, P.
709 Impact of 2004 tsunami on seafloor morphology and offshore sediments, Pakarang Cape, Thailand,
710 Polish Journal of Environmental Science Vol. 18, No. 1, 63-68, 2009.
711 16) Fujino S., Naruse H., Matsumoto, D., Jarupongsakul T., Sphawajruksakul A., and Sakakura, N.:
712 Stratigraphic evidence for pre–2004 tsunamis in southwestern Thailand, Marine Geology, 262, 25–
713 28, 2009.
714 17) Fujino, S., Naruse, H., Matsumoto, D., Sakakura, N., Suphawajruksakul, A., and Jarupongsakul,
715 T.: Detailed measurements of thickness and grain size of a widespread onshore tsunami deposit in
716 Phang–nga Province, southwestern Thailand, Island Arc, 19, 389–398, 2010.

717 18) Gelfenbaum G., Vatvani D., Jaffe B., and Dekker F.: Tsunami inundation and sediment transport
718 in vicinity of coastal mangrove forest, Coastal Sediments, 07, 1117-1128, 2007.
719 19) Goto, K., Takahashi, J., Oie, T., and Imamura, F.: Remarkable bathymetric change in the nearshore
720 zone by the 2004 Indian Ocean tsunami: Kirinda Harbor, Sri Lanka, Geomorphology, 127, No.1-
721 2, 107–116, 2011a.
722 20) Goto, K., ChaguéGoff, C., Fujino, S., Goff, J., Jaffe B., Nishimura, Y., Richmond, B., Sugawara,
723 D., Szczuciński, W., Tappin, R. D., Witter, C. R., and Yuliant, E., New insights of tsunami hazard
724 from the 2011 Tohoku–oki event, Marine Geology, 290, 46–50, 2011b.
725 21) Goto, K., Chague´Goff, C., Goff, J., and Jaffe, B.: The future of tsunami research following the
726 2011 Tohoku–oki event, Sedimen- tary Geology, 282, 1–13, 2012.
727 22) Gouramanis, C., Switzer, A. D., Polivka, P. M., Bristow, C. S., Jankaew, K., Dat, P. T., Pile, J.,
728 Rubin, C. M., Yingsin, L., Ildefonso, S. R., and Jol, H. M.: Ground penetrating radar examination
729 of thin tsunami beds - A case study from Phra Thong Island, Thailand,Sediment. Geol., 329, 149–
730 165, 2015.
731 23) Gouramanis, C., Switzer, A. D., Jankaew, K., Bristow, C. S., Pham, D. T., and Ildefonso, S. R.:
732 High-frequency coastal overwash deposits from PHRA thong Island, Thailand, Sci. Rep., Vol.7,
733 No. September 2016, 1–9, 2017.
734 24) Gusman, A. R., Tanioka, Y., and Takahashi, T.: Numerical experiment and a case study of sediment
735 transport simulation of the 2004 Indian Ocean tsunami in Lhok Nga, Banda Aceh, Indonesia., Earth,
736 planets and space, 64, 817-827, 2012.
737 25) Haraguchi, T., Takahashi, T., Hisamatsu, R., Morishita, Y., and Sasaki, I.: A Field Survey of
738 Geomorphic Change on Kessennuma Bay caused by the 2010 Chilean Tsunami and the 2011
739 Tohoku Tsunami, Journal of JSCE, B2 (Coastal Engineering), 68, 231–235, 2012.
740 26) Hawkes, A.D., Bird, M., Cowie, S., Grundy-Warr, C., Horton, B.P., Hwai, A.T.S., Law, L.,
741 Macgregor, C., Nott, J., Ong, J.E., Rigg, J., Robinson, R., Tan-Mullins, M., Sa, T.T., Yasin, Z., Aik,
742 L.W.: Sediments deposited by the 2004 Indian Ocean Tsunami along the Malaysia–Thailand
743 Peninsula, Marine Geology, 242, 169–190, 2007.
744 27) Hirao, R., Tanaka, H., Umeda, M., Adityawan, M. B., Mano, A., and Udo, K.: Breaching of Sandy
745 Coast and Spit Due To The 2011 Tsunami and Their Recovery, Journal of JSCE, B2(Coastal
746 Engineering), 68, 581–585, 2012.
747 28) Imai, K., Sugawara, D., Takahashi, T., Iwama, S., and Tanaka, H.: Numerical study for sediment
748 transport due to tsunami around the Kitakami River mouth, Journal of JSCE, B2(Coastal
749 Engineering), 71, 247–252, 2015.
750 29) Imamura, F.: Review of tsunami simulation with a finite difference method, in: Long-Wave Runup
751 Models, edited by: Yeh, H., Liu, P., and Synolakis, C. E., World Scientific Publishing Co.,
752 Singapore, 25–42, 1996.
753 30) Iwagaki, Y.: Hydrodynamical study on critical tractive force, Trans. JSCE, 41(41), 1–21, 1956.
754 31) Jaffe, B., Goto, K., Sugawara, D., Gelfenbaum, G., and La Selle, S.: Uncertainty in tsunami

755 sediment transport modeling. Journal of Disaster Research, 11(4), 647-661, 2016.
756 32) Jankaew, K., Atwater, B. F., Sawai, Y., Choowong, M., Charoentitirat, T., Martin, M. E., and
757 Prendergast, A.: Medieval forewarning of the 2004 Indian Ocean tsunami in Thailand, Nature,
758 455(7217), 1228–1231, 2008.
759 33) Koiwa, N., Takahashi, M., Sugisawa, S., Ito, A., Aki Matsumoto, H., Tanavud, C., and Goto, K.:
760 Barrier spit recovery following the 2004 Indian Ocean tsunami at Pakarang Cape, southwest
761 Thailand, Geomorphology, 306, 314–324, 2018.
762 34) Land Development Department of Thailand (LDD) Maps and mapping information, Available at:
763 http://www.ldd.go.th/www/lek_web/web.jsp?id=19273 (Accessed date: 18 October 2017)
764 35) Li, L., Qiu, Q., and Huang, Z.: Numerical modeling of the morphological change in Lhok Nga,
765 west Banda Aceh, during the 2004 Indian Ocean tsunami: understanding tsunami deposits using a
766 forward modeling method, Natural Hazards, 64, 1549-1574, 2012.
767 36) Li, L., Huang, Z., and Qiu, Q.: Numerical simulation of erosion and deposition at the Thailand
768 Khao Lak coast during the 2004 Indian Ocean tsunami, Natural Hazards, 74, 2251-2277, 2014.
769 37) Liew, S.C., Gupta, A., Wong, P.P., Kwoh, L.K.: Recovery from a large tsunami mapped over time:
770 The Aceh coast, Sumatra, Geomorphology, 114, 520–529, 2010.
771 38) Morishita, Y., and Takahashi, T.: Accuracy improvement of movable bed model for tsunamis by
772 applying for Kesennuma bay when the 2011 Tohoku tsunami arrived, Journal of JSCE, B2(Coastal
773 Engineering), 70, 491–495, 2014.
774 39) Rubey, W. W.: Settling velocity of gravel, sand, and silt particles. American Journal of Science,
775 148, 325-338, 1933.
776 40) Saegusa, S., Tanaka, H., and Mitobe, Y.: Recovery processes of bathymetry of Sendai Bay after the
777 2011 tsunami, Journal of JSCE, B2(Coastal Engineering), 73, 817–822, 2017.
778 41) Okada, Y.: Surface deformation due to shear and tensile faults in a half-space, Bulletin of the
779 Seismological Society of America, 75(4), 1135–1154, 1985.
780 42) Pari, Y., Ramana Murthy, M. V., Jaya Kumar, S., Subramanian, B. R., and Ramachandran, S.:
781 Morphological changes at Vellar estuary, India — Impact of the December 2004 tsunami, Journal
782 of Environmental Management, 89, 45–57, 2008.
783 43) Paris, R., Lavigne, F., Wassmer, P., Sartohadi, J.: Coastal sedimentation associated with the
784 December 26, 2004 tsunami in Lhok Nga, west Banda Aceh (Sumatra, Indonesia), Marine Geology,
785 238, 93–106, 2007.
786 44) Pham, T. D., Gouramanis, C., Switzer, M. A., Rubin, M. C., Jones, G. B., Jankaew, K., and Carr,
787 F. P.: Elemental and mineralogical analysis of marine and coastal sediments from Phra Thong
788 Island, Thailand: Insights into the provenance of coastal hazard deposits, Marine Geology, 385,
789 274–292, 2018.
790 45) Prendergast, L. A., Cupper L. M., Jankaew, K., and Sawai, Y.: Indian Ocean tsunami recurrence
791 from optical dating of tsunami sand sheets in Thailand, Marine Geology, 295–298, No.15, 20–27,
792 2012.

793 46) Sawai, Y., Jankaew K., Martin, E. M., Prendergast, A., Choowong, M., and Charoentitirat, T.:
794 Diatom assembles in tsunami deposits associated with th 2004 Indian Ocean tsunami at Phra Thong
795 Island, Thailand, Marine Micropaleontology, 73, 70–79, 2009.
796 47) Sugawara, D., Goto, K., and Jaffe, B. E.: Numerical models of tsunami sediment transport –Current
797 understanding and future directions, Marine Geology, 352, 295–320, 2014a.
798 48) Sugawara, D., Takahashi, T., and Imamura, F.: Sediment transport due to the 2011 Tohoku-oki
799 tsunami at Sendai: Results from numerical modeling, Mar. Geol., 358, 18–37, 2014b.
800 49) Suppasri, A., Koshimura, S., and Imamura, F.: Developing tsunami fragility curves based on the
801 satellite remote sensing and the numerical modeling of the 2004 Indian Ocean tsunami in Thailand,
802 Nat. Hazards Earth Syst. Sci., 11(1), 173–189, 2011.
803 50) Suppasri, A., Latcharote, P., Bricker, J. D., Leelawat, N., Hayashi, A., Yamashita, K., Makinoshima,
804 F., Roeber, V. and Imamura, F.: Improvement of tsunami countermeasures based on lessons from
805 the 2011 great east japan earthquake and tsunami -Situation after five years-, Coastal Engineering
806 Journal, 58 (4), 1640011, 2016.
807 51) Switzer, A.D., Srinivasalu, S., Thangadurai, N., Ram Mohan, V.: Bedding structures in Indian
808 tsunami deposits that provide clues to the dynamics of tsunami inundation, Geological Society,
809 London, Special Publications, 361, 61-77, 2012.
810 52) Szczuciński, W., Kokociński, M., Rzeszewski, M., Chahué–Goff, C., Cachão, M., Goto, K., and
811 Sugawara, D.: Sediment sources and sedimentation processes of 2011 Tohoku–oki tsunami
812 deposits on the Sendai Plain, Japan — Insights from diatoms, nannoliths and grain size distribution,
813 Sedimentary Geology, 282, 40–56, 2012.
814 53) Takahashi, T., Shuto, N., Imamura, F., and Asai, D.: Modeling sediment transport due to tsunamis
815 with exchange rate between bed load layer and suspended load layer, Proceedings Of International
816 Conference of Coastal Engineering, 1508–1519, 2000.
817 54) Takahashi, J., Goto, K., Oie, T., Yanagisawa, H., and Imamura, F.: Inundation and topographic
818 Change due to the 2004 Indian Ocean Tsunami at the Kirinda port, Sri Lanka, Journal of JSCE,
819 B2(Coastal Engineering), 55, 251–255, 2008.
820 55) Takahashi, T., Kurokawa, T., Fujita, M., and Shimada, H.: Hydraulic experiment on sediment
821 transport due to tsunamis with various sand grain size, Journal of JSCE, B2(Coastal Engineering),
822 67, 231–235, 2011.
823 56) Takahashi, T.: Numerical modeling if sediment transport due to tsunamis and its problem, Journak
824 of the Sedimentological Society of Japan, 71, 2, 149-155, 2012.
825 57) Takashimizu, Y., Urabe, A., Suzuki, K., and Sato, Y.: Deposition by the 2011 Tohoku–oki tsunami
826 on coastal lowland controlled by beach ridges near Sendai, Japan, Sedimentary Geology, 282, 124–
827 141, 2012.
828 58) Tanaka, H., Ishino, K., Nawarathna, B., Nakagawa, H., and Yano, S.: Coastal and river mouth
829 morphology change in Sri Lanka due to the 2004 Indian Ocean Tsunami. In Coastal Sediments' 07
830 (pp. 842-855), 2007.

831 59) Tanaka, H., Mano, A., and Udo, K.: Beach Morphology Change Induced by The 2011 Great East
832 Japan Earthquake Tsunami, Journal of JSCE, B2(Coastal Engineering), 67(2), 571–575, 2011.
833 60) Udo, K., Tanaka, H., Mano, A., and Takeda, Y.: Beach Morphology Change of Southern Sendai
834 Coast due to 2011 Tohoku Earthquake Tsunami, Journal of JSCE, B2(Coastal Engineering), 69,
835 391–395, 2013.
836 61) Udo, K., and Takeda, Y.: Comparison between characteristics of shoreline changes due to the 2004
837 Indian Ocean tsunami and the 2011 Great East Japan tsunami, Journal of JSCE, B3(Coastal
838 Engineering), 72, 175–180, 2016.
839 62) Van Rijn, L. C.: Unified view of sediment transport by currents and waves. I: Initiation of motion,
840 bed roughness, and bed-load transport. Journal of Hydraulic engineering, 133(6), 649-667, 2007.
841 63) Watanabe, A., Maruyama, Y., Shimizu, T., and Sakakiyama, T.: Numerical prediction model of
842 three-dimensional beach transformation due to installed structures, Journal of JSCE(Coastal
843 Engineering), 31, 406–410, 1984.
844 64) Watanabe, M., Goto, K., Bricker, J. D., and Imamura, F.: Are inundation limit and maximum extent
845 of sand useful for differentiating tsunamis and storms? An example from sediment transport
846 simulations on the Sendai Plain, Japan. Sedimentary geology, 364, 204-216, 2018.
847 65) Xu, J.: Grain-size characteristics of suspended sediment in the Yellow River, China, Catena, 38,
848 243-263, 1999a.
849 66) Xu, J.: Erosion caused by hyperconcentrated flow on the Loess Plateau of China, Catena, 36, 1-19,
850 1999b.
851 67) Yamashita, K., Sugawara, D., Takahashi, T., Imamura, F., Saito, Y., Imato, Y., Kai, T., Uehara, H.,
852 Kato, T., Nakata, K., Saka, R., and Nishikawa, A.: Numerical simulation of large-scale sediment
853 transport due to the 2011 tohoku earthquake tunami in Rikuzentakata city, Journal of JSCE,
854 B2(Coastal Engineering), 71, 499–504, 2015.
855 68) Yamashita, K., Sugawara, D., Takahashi, T., Imamura, F., Saito, Y., Imato, Y., and Saka, R.:
856 Numerical simulations of large-scale sediment transport caused by the 2011 Tohoku Earthquake
857 Tsunami in Hirota Bay, Southern Sanriku Coast. Coastal Engineering Journal, 58(04), 2016.
858 69) Yamashita, K., Shigihara , Y., Sugawara, D., Arikawa, T., Takahashi, T., and Imamura, F.: Effect of
859 sediment tansport on tsunami hazard and building damage –an integrated simulation of tsunami
860 inundation, sediment transport and drifting vessels in Kesennuma city, Miyagi prefecture during
861 the great east Japan –, Journal of JSCE, B2(Coastal Engineering), 73, 355–360, 2017.
862 70) Yamashita, K., Sugawara, D., Arikawa, Y.., Takahashi, T., and Imamura, F.: Improvement of
863 tsunami-induced sediment transport model by considering saturated concentration in suspension
864 with strong unsteady flows, Journal of JSCE, B2(Coastal Engineering), 69, 325–330, 2018.
865 71) Yunus Ali, P., and Narayama, A. C.: Short–Term Morphological and Shoreline Changes at Trinkat
866 Island, Andaman and Nicobar, India, After the 2004 Tsunami, Marine Geodesy, 38, 26–39, 2015.
867